Submitted to *Chemistry of Materials* *March 18, 2017*

Correlating local compositions and structures with the macroscopic optical properties of Ce^{3+}-doped $CaSc_2O_4$, an efficient green-emitting phosphor

Nathan C. George,[†,⊥] Jakoah Brgoch,[⊥,€] Andrew J. Pell,[‡,¶] Clayton Cozzan,[⊥] Adam Jaffe,[⊥,£] Géraldine Dantelle,[§] Anna Llobet,[$] Guido Pintacuda,[‡] Ram Seshadri[⊥,*] Bradley F. Chmelka,[†,*]

[†] Department of Chemical Engineering, University of California, Santa Barbara, California, 93106, U.S.A.

[⊥] Materials Department and Materials Research Laboratory, University of California, Santa Barbara, California, 93106, U.S.A.

[‡] Centre de RMN à Très Hauts Champs, Université de Lyon, Institute of Analytical Sciences, CNRS/Ecole Normale Supérieure de Lyon/Université Claude Bernard Lyon 1, 5 rue de la Doua, 69100 Villeurbanne, France

[§] Institut Néel CNRS, UPR 2940/Université Grenoble Alpes, 25 Av. des Martyrs, 38 042 Grenoble Cedex 09, France

[$] Lujan Neutron Scattering Center, Los Alamos National Laboratory, New Mexico 87545, U.S.A.

* To whom correspondence should be addressed: bradc@engineering.ucsb.edu; seshadri@mrl.ucsb.edu

[£] Present address: Department of Chemistry, Stanford University, Stanford, California 94305, U.S.A.

[€] Present address: Department of Chemistry, University of Houston, Houston, Texas 77204, U.S.A.

[¶] Present address: Department of Materials and Environmental Chemistry, Arrhenius Laboratory, Stockholm University, Svante Arrhenius Väg 16 C, SE-106 91 Stockholm, Sweden

Abstract

Calcium scandate ($CaSc_2O_4$) substituted with small amounts (<1%) of Ce^{3+} is a recently discovered bright green-emitting phosphor with favorable light absorption and emission properties and robust temperature stability that make it well-suited for solid-state white-lighting applications. Combined analyses of scattering, solid-state nuclear magnetic resonance (NMR), electron spin resonance (ESR), and photoluminescence measurements establish the compositional and structural origins of the macroscopic optical properties of this phosphor material. Simultaneous refinements of synchrotron X-ray and neutron diffraction data of Ce^{3+}-doped $CaSc_2O_4$ enable the average crystal structure to be determined, which is shown to correspond to an exceedingly rigid host structure, as corroborated by density functional theory (DFT) calculations. Such structural rigidity leads to high quantum efficiency, which is optimized by the substitution of as little as 0.5 mol% of Ce^{3+} for Ca^{2+} ions, with higher extents of Ce^{3+} substitution leading to decreased photoluminescent quantum yields (PLQY). Solid-state ^{43}Ca and ^{45}Sc magic-angle spinning (MAS) NMR spectra are sensitive to the effects of the paramagnetic Ce^{3+} dopant ions on nearby atoms in the host structure and yield evidence for local structural distortions. ESR measurements provide direct insights on structures of the Ce^{3+} ions, as a function of Ce^{3+} substitution. The combined scattering and spectroscopic analyses yield detailed new understanding of the local and long-range structures of Ce^{3+}-doped $CaSc_2O_4$, which account for the sensitive composition-dependent optical properties of this important phosphor material.

INTRODUCTION

The advantages of solid-state lighting (SSL) over conventional light sources include mercury-free materials, physically robust devices, long lifetimes, and high efficiencies.[1,2] SSL devices generally yield white light from a blue or near-UV light-emitting diode (LED) by using an inorganic phosphor, such as Ce^{3+}-doped $Y_3Al_5O_{12}$ (yttrium-aluminum-garnet, YAG) or calcium scandate ($CaSc_2O_4$), to partially down-convert blue or UV LED emission to longer wavelengths; the combined emission appears as white light. Several design and performance criteria govern selection of phosphor materials for SSL applications. Ideal materials have high quantum efficiencies, good chemical stabilities, as well as excitation and emission bands that are compatible with commercially available LEDs.[3] High efficiencies, even at elevated temperatures (≈500 K), make them suitable for high-power lighting devices.[4] Currently, the most widely investigated compound that meets these design criteria for white-light phosphors is cerium-substituted YAG, (YAG:Ce^{3+}).[5] Although progress has been made in the development of this and other oxide phosphors for SSL, phosphors with outstanding optical properties are still sought, and the atomic-level origins of their properties remain poorly understood.[5] To complement the general criteria for high performance described above, additional design rules are sought that will enable the identification of new candidate phosphors with improved photoluminescence properties.

The pursuit of thermally stable phosphors with high quantum yields has recently focused on materials with dense polyhedral bonding networks.[6] Structures with dense packing of polyhedral units tend to have rigid bonding networks that prevent non-radiative relaxation from excited states (*e.g.*, via vibrational relaxation). One phosphor that fulfills the design criteria for high efficiency is Ce^{3+}-substituted $CaSc_2O_4$, the preparation of which has been reported by using a variety of methods, including laser-heated pedestal growth,[7,8] combustion synthesis,[9] or conventional high-temperature methods.[10] This host material ($CaSc_2O_4$) has also been made luminescent by doping

with Eu^{2+},[11] Er^{3+},[12] Ho^{3+},[13] Tm^{3+},[14] and by co-doping Ce^{3+} with $Tm^{3+}/La^{3+}/Tb^{3+}$,[15] and Yb^{3+}.[16] It has also been investigated for use as an up-conversion phosphor.[17–20] Based on X-ray scattering analyses,[21] the host structure, $CaSc_2O_4$, depicted in Figure 1, contains distorted ScO_6 octahedra that form a three-dimensional network of edge- or corner-sharing polyhedra. Moreover, the high charge-to-radius ratio of the 8-coordinated Ca^{2+} site provides additional rigidity to the structure that should further improve the photoluminescent quantum yield (PLQY) of the compound.[6] Substituting Ce^{3+} cations into the Ca^{2+} site results in bright green luminescence,[22] because the ionic radius of Ca^{2+} (1.12 Å; 8-coordinate) is smaller than that of Ce^{3+} (1.143 Å; 8-coordinate).[23] Such substitution also requires charge compensation, which may be provided by interstitial oxygen or fluorine atoms (sometimes halide salts are used as fluxes in phosphor syntheses), or Sc/Ca vacancies.[24] The substitution of larger Ce^{3+} luminescent cations into the smaller Ca^{2+} site forces considerable crystal field splitting that leads to the observed green emission. $CaSc_2O_4:Ce^{3+}$ is efficiently excited across a wide range of wavelengths from 400 nm to 475 nm and emits broadly from 475 nm to 625 nm, making it suitable as a green component in SSL devices. Furthermore, $CaSc_2O_4:Ce^{3+}$ has been shown to retain high photoluminescence intensity even at elevated temperatures, with only a 25% decrease in emission intensity at 453 K compared to room temperature,[10] and a quantum yield measured to be over 80% at room temperature for the materials studied here. The scattering analyses and average structures of different $Ca_{1-x}Ce_xSc_2O_4$ phosphor materials alone, however, provide few insights on the origins of their interesting photoluminescence properties, so other techniques are required.

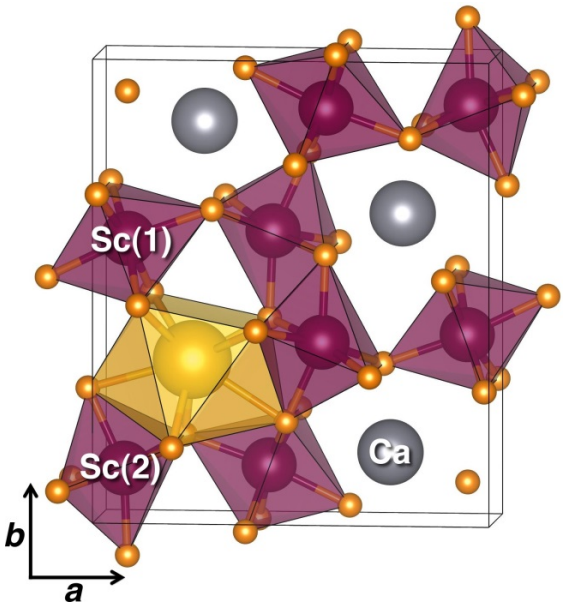

Figure 1. Schematic diagram of the crystal structure of the phosphor $Ca_{1-x}Ce_xSc_2O_4$, with the cations labeled. The small orange spheres represent oxygen atoms, and the large gold sphere corresponds to a Ce^{3+} ion substituted into a Ca^{2+} site.

Here, we present a comprehensive study of structure-property relationships for the new solid-state phosphor, $CaSc_2O_4:Ce^{3+}$. The absolute PLQY of the green-emitting $CaSc_2O_4:Ce^{3+}$ phosphor was determined for very dilute Ce^{3+} substitutions ranging from 0.5% to 1.5%. A careful analysis of the average crystal structure, as well as the local structures near the luminescent Ce^{3+} centers, was conducted and correlated with the macroscopic optical properties of the material. The average crystal structure of $CaSc_2O_4:Ce^{3+}$ was characterized by using synchrotron X-ray and neutron scattering techniques and found to correspond to a structurally robust lattice, as estimated by the Debye temperature and consistent with the high quantum yield of the phosphor. These results were correlated with solid-state nuclear magnetic resonance (NMR) and electron spin resonance (ESR) spectroscopy measurements to measure and understand how Ce^{3+} cations affect the $CaSc_2O_4$ host structure. By focusing on the interplay between structural rigidity and changes in local symmetry due to Ce^{3+} substitution, we establish the atomic-scale origins of the superior

photoluminescent properties for a very dilute Ce^{3+}-doped material with the optimized composition $Ca_{0.995}Ce_{0.005}Sc_2O_4$.

EXPERIMENTAL SECTION

Materials syntheses. Samples of $Ca_{1-x}Ce_xSc_2O_4$ (x = 0, 0.005, 0.0075, 0.01, 0.015) were prepared by using high-temperature methods. The desired stoichiometric ratios of starting materials $CaCO_3$ (Fisher Scientific, ≥99%), Sc_2O_3 (Stanford Materials Corp., >99.99%), and CeO_2 (Cerac, 99.9%) were ground in an agate mortar and pestle, placed in alumina crucibles, and fired at 1600 °C for 6 h in an alumina tube furnace under 0.2 L/min 5% H_2/95% N_2 gas flow. Although the substitution of trivalent Ce^{3+} for divalent Ca^{2+} is expected to lead to cation or anion defects to maintain charge neutrality, because of the low nominal Ce^{3+} contents, the influences on the bulk compositions of the materials will be small; thus, the bulk compositions herein are considered to be $Ca_{1-x}Ce_xSc_2O_4$. After the starting materials had reacted, the products were ground with an agate mortar and pestle into fine powders.

Optical characterization measurements. Photoluminescence spectra were obtained at room temperature on a Horiba Fluoromax-4 spectrophotometer with a Quantum-Φ 150 mm Spectralon™-coated integrating sphere attachment. The powdered sample was encapsulated in silicone resin (GE Silicones, RTV615) and deposited on a silica substrate (Chemglass). The excitation light was produced by a 150 W xenon arc lamp. Photoluminescent quantum yields (PLQY) were determined following the method of de Mello, *et al*.[25]

Temperature-dependent photoluminescence. The temperature dependence of the PL properties was studied on a home-made fluorimeter that consisted of a laser excitation source (457 nm) and Czerny-Turner monochromator (Acton SpectraPro-500) equipped with a charge-coupled device (CCD) camera (Princeton Instruments PIXIS:400). Corrections for variations in spectral response were determined by measuring the spectrum of the Ocean Optics calibration light source

(Ocean Optics LS-1) with near-black body emission spectrum and applied to the spectra collected. PL measurements were conducted over the range 77 K to 375 K in a liquid-nitrogen cryostat (Janis Research VPF-100) with a Lakeshore 321 temperature controller and using an Instec ST200E heating stage over the range 303 K to 375 K.

Synchrotron X-ray and neutron scattering. High-resolution synchrotron X-ray powder diffraction data were collected on the 11-BM beamline at the Advanced Photon Source (APS) at Argonne National Laboratory, using an average wavelength of λ = 0.413531 Å. Other details regarding the experimental setup can be found elsewhere.[26] Neutron powder diffraction was performed on the HIPD instrument at the Lujan Neutron Scattering Center at Los Alamos National Laboratory. Powder samples were placed in vanadium cans, and time-of-flight neutron data were collected at 295 K from 8 detector banks at 2Θ values of ±14°, ±40°, ±90°, and ±153°. Crystal structures were refined by using the EXPGUI[27] front end for the refinement program General Structure Analysis System (GSAS).[28] Simultaneous refinements to the X-ray and neutron scattering data were completed by adjusting the profile shapes and unit cells during LeBail fits, refining neutron absorption coefficients, instrument parameters, and the backgrounds (10-term shifted-Chebyshev polynomial function), then refining the atomic positions, and finally the atomic displacement parameters. During the final refinement cycle, all appropriate free parameters were allowed to refine simultaneously. Crystal structures were visualized using the software VESTA.[29]

Solid-state NMR spectroscopy. High-resolution solid-state ^{43}Ca and ^{45}Sc NMR spectroscopy was used to investigate the local compositions and structural environments of calcium and scandium atoms in the $Ca_{1-x}Ce_xSc_2O_4$ materials. Solid-state ^{45}Sc (nuclear spin I=7/2, 100% natural abundance) NMR spectra were acquired on a Bruker Advance III 1 GHz spectrometer at 23.5 T, operating at a ^{45}Sc Larmor frequency of 243 MHz, with a 1.3 mm HX probehead under conditions of magic-angle spinning (MAS) at 60 kHz. One-dimensional (1D) ^{45}Sc NMR spectra were acquired by direct

excitation of ^{45}Sc nuclei by using a one-pulse sequence with an excitation pulse of 44.6 kHz radiofrequency (RF) field amplitude and 1.4 μs duration. Spin-lattice (T_1) relaxation times were measured by using a saturation-recovery experiment comprised of a saturation sequence of 50 pulses separated by delays of 3 ms and a variable recovery delay taking 20 values from 10 ms to 60 s. Quantitative 1D spectra were acquired using a one-pulse sequence with 64 scans and recycle delays of 54.4 s (x = 0), 53.6 s (x = 0.005), 48.7 s (x = 0.010), and 43.5 s (x = 0.015). All ^{45}Sc shifts were referenced to a 1 M aqueous solution of $Sc(NO_3)_3$. Additional ^{45}Sc NMR spectra were acquired with a higher repetition rate to filter ^{45}Sc signals based on their T_1 relaxation times. For such spectra, 32768 transients were acquired with a recycle delay of 100 ms to enhance the signals from faster-relaxing ^{45}Sc nuclei in close proximity to paramagnetic Ce^{3+} cations, which therefore exhibit shorter T_1 values. Two-dimensional (2D) ^{45}Sc MQMAS spectra[30] were acquired by using a triple-quantum (3Q) pulse sequence with a z-filter.[31] The 3Q excitation pulse and the pulse used to convert triple-quantum coherence back to z-magnetization had RF field amplitudes of 141 kHz and were applied for 1.5 μs and 0.5 μs, respectively. The final low-power 90° pulse had a 44.6 kHz RF field amplitude and a duration of 1.4 μs. The time increment in the indirect dimension was 50 ms, and 64 increments were acquired using the States-Haberkorn-Rubens method to obtain pure-phase line shapes and frequency discrimination.[32] 96 transients were acquired per t_1 increment. The data were sheared in the time domain during processing.[33] Spectra were acquired without active temperature control for all materials, resulting in an estimated sample temperature of 360 K. To assess the temperature-dependence of the paramagnetically displaced ^{45}Sc signals, a spectrum of one material (x = 0.015) was acquired by using a variable temperature Bruker BCU-X cooling unit with a N_2 flow of 1335 L/hr and a set-point of 243 K, resulting in an estimated sample temperature of 300 K under the fast MAS (60 kHz) conditions used. Solid-state NMR spectra were modeled and the NMR parameters were extracted by using the simulation program DMFIT.[34]

Solid-state ^{43}Ca (nuclear spin I=7/2, 0.145% natural abundance) NMR spectra were acquired at the U.S. National High Magnetic Field Laboratory in Tallahassee, Florida on a narrow-bore Magnex 19.6 T magnet with a Bruker console, operating at a ^{43}Ca Larmor frequency of 56.067 MHz. The measurements were collected at room temperature under MAS conditions of 6 kHz using a Samoson 7 mm HX triple-resonance MAS probehead with zirconia rotors and Kel-F™ caps. RF pulses with a 1.5 μs length were used with a recycle delay of 5 s, and 8000 transients were acquired. All ^{43}Ca shifts were referenced to 1 M $CaCl_2$ (*aq*).

Electron Paramagnetic Resonance (EPR) spectroscopy. EPR spectra were collected on a Bruker X-Band EPR spectrometer (ν = 9.486 GHz) equipped with a helium flow cryostat. Samples were placed in silica tubes, and spectra were acquired at 4 K and with 6309 mW microwave power. Spectral simulations employed the EASYSPIN code implemented in MATLAB,[35] with a correction included for field-dependent relaxation effects.

RESULTS AND DISCUSSION

The substitution of low concentrations of rare-earth cations, *e.g.*, Ce^{3+}, into calcium scandate ($CaSc_2O_4$) leads to materials with efficient photoluminescent properties. This arises, in part, due to the larger atomic radius of Ce^{3+}, compared to the smaller Ca^{2+} cation, leading to significant crystal field splitting. The result is a shift of the absorption bands to longer wavelengths when $CaSc_2O_4$:Ce^{3+} is excited between >400 nm and 475 nm (maximum intensity at λ_{max} = 455 nm), as manifested by a small Stokes shift of ≈60 nm and emission across the green-yellow region of the visible spectrum (λ_{max} = 515 nm), as shown in Figure 2a. The photoluminescence quantum yield in the $Ca_{1-x}Ce_xSc_2O_4$ system can be optimized by varying the extent of Ce^{3+} substitution over a narrow and dilute range, e.g., x = 0 to 0.015, leading to a high quantum yield of 85% when 0.5% of Ce^{3+} (x = 0.005) was substituted into calcium scandate (Figure 2b, spectra in Supporting Information, Figure S2). Interestingly, the quantum yield decreased dramatically to 60% and 31% with substitution of

modestly higher loadings of 1% Ce^{3+} and 1.5% Ce^{3+}, respectively. Such an abrupt decrease in the PLQY with increasing Ce^{3+} is likely to be due to either structural distortions arising from incorporation of the larger Ce^{3+} ions into smaller Ca^{2+} sites or the formation of anionic defects stemming from charge imbalance; these both inhibit photoemission and are consistent with the lower quantum yields observed. The optical properties of these materials, furthermore, exhibit high thermal stabilities, as manifested by temperature-dependent photoluminescence spectra and analyses shown in Supporting Information, Figure S3.

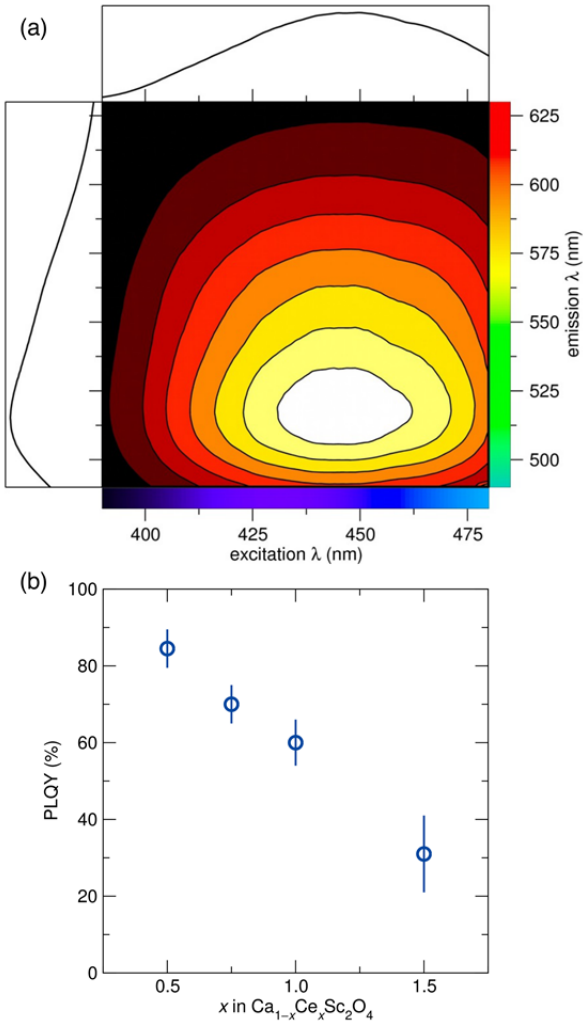

Figure 2. (a) Two-dimensional excitation and emission scans of $Ca_{0.995}Ce_{0.005}Sc_2O_4$ phosphor. The most intense excitation and emission spectra are shown above and beside the plot, respectively. (b) Plot of photoluminescence quantum yield (PLQY) measured at room temperature for λ_{ex} = 445 nm for $Ca_{1-x}Ce_xSc_2O_4$ phosphors with different Ce contents x=0.005, 0.0075, 0.010, and 0.015. The uncertainty bars represent distributions over multiple measurements.

Average crystal structure and optical response of $CaSc_2O_4$:Ce^{3+}. As reported previously,[21] the undoped $CaSc_2O_4$ host material has an orthorhombic crystal structure (Figure 1, space group *Pnam*) with one Ca^{2+} site, two Sc^{3+} sites, and four O^{2-} sites. The two Sc^{3+} ions are in the centers of distorted octahedra with the $Sc(1)O_6$ units and $Sc(2)O_6$ units sharing edges. The substitution of Ce^{3+} into the $CaSc_2O_4$ crystal structure occurs only at the Ca^{2+} site, due to size constraints. This result has similarly been observed by extended X-ray absorption fine structure (EXAFS) measurements for the analogous garnet system, $Ca_3Sc_2Si_3O_{12}$:Ce^{3+}.[36]

For calcium scandate containing low loadings of Ce^{3+} dopant ions (<2% substitution), the bulk orthorhombic crystal structure and space group are retained. For example, Figure 3 shows representative synchrotron X-ray and neutron scattering patterns for the material with the composition $Ca_{0.995}Ce_{0.005}Sc_2O_4$, all reflections of which are indexable to the *Pnam* structure, indicating a single-phase product. Rietveld refinements of these data support the previously determined crystal structure[21] and provide general insights on the average structure and thermal-mechanical properties of the $Ca_{1-x}Ce_xSc_2O_4$ phosphor materials. For example, the synchrotron X-ray scattering analysis (Figure 3a) allows the variation of the average unit cell parameters to be accurately determined, as functions of small amounts of substituent atoms, such as Ce^{3+}. For the unsubstituted $CaSc_2O_4$ material, the unit cell parameters and fit quality indicators associated with Rietveld refinement of synchrotron X-ray data (Table 1) agree well with previous X-ray diffraction studies of $CaSc_2O_4$.[21,37,38] The substitution of Ce^{3+} induces a small (<1%) expansion of the unit cell that is consistent with 8-coordinate Ce^{3+} being slightly larger than Ca^{2+}. The unit cell parameters of $Ca_{1-x}Ce_xSc_2O_4$, monitored as a function of Ce^{3+} content over the range x = 0 to 0.01, suggest a maximum for Ce^{3+} substitution above x = 0.005, which could be due to a solid-solution limit, or from charge imbalance between Ca^{2+} and Ce^{3+}, which may lead to the formation of defects.

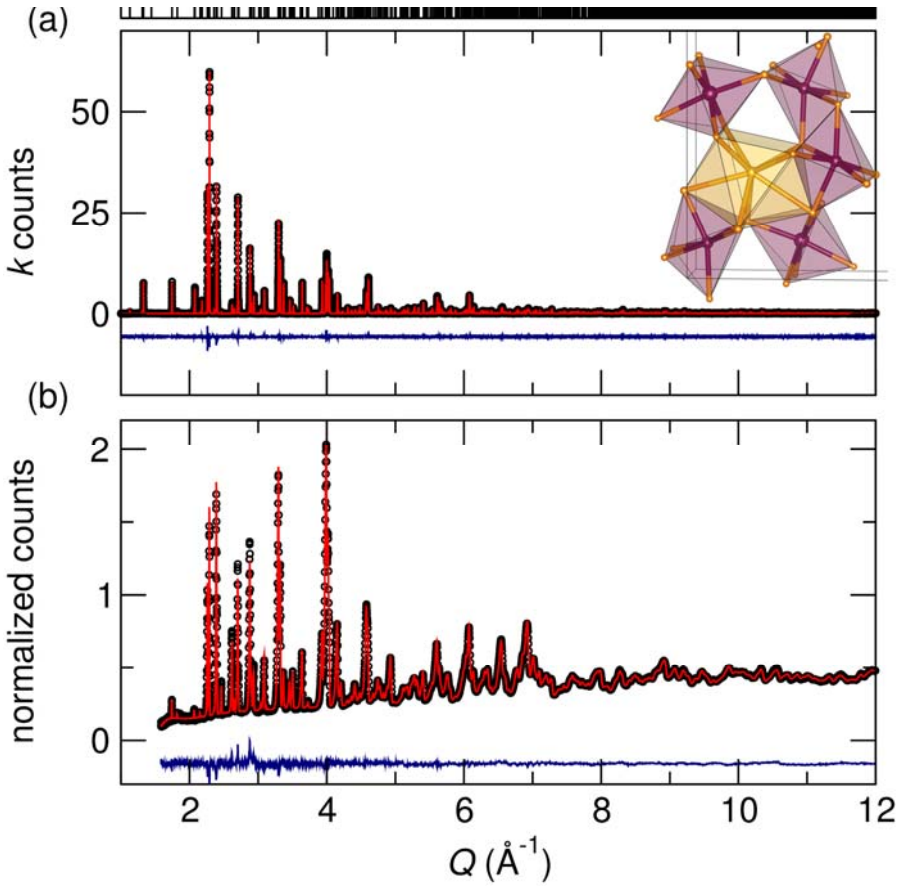

Figure 3. Simultaneous Rietveld refinement of the (a) synchrotron X-ray scattering data and (b) time-of-flight neutron scattering data acquired at 295 K for the phosphor $Ca_{0.995}Ce_{0.005}Sc_2O_4$. The expected reflection positions are shown above the plots. The inset in (a) is a part of the crystal structure, depicted with 99% probability thermal ellipsoids from the refinement. Note the exceedingly small ellipsoids, which reflect the rigidity of the structure. The same sample was used in Figures 2a, 5, and 7.

Table 1. Parameters from combined Rietveld refinements of $Ca_{1-x}Ce_xSc_2O_4$ of synchrotron X-ray and neutron powder diffraction data.

x	0	0.005	0.01
Crystal System		Orthorhombic	
Space Group; Z		*Pnma*; 4	
Temperature		295 K	
a (Å)	9.46337(1)	9.463453(9)	9.463452(9)
b (Å)	11.11158(1)	11.11176(1)	11.11176(1)
c (Å)	3.141928(4)	3.142051(3)	3.142052(3)
V (Å^3)	330.3831(7)	330.4043(6)	330.4043(6)
X-ray R_{wp} (%)	10.5	8.17	8.16
neutron R_{wp} (%)	1.56	1.58	1.59

Based on the scattering data available, however, it is not possible to determine the occupancies of Ce^{3+} ions within the phosphor structure, due to the low extents of substitution (≤1.5%) and the lack of long-range Ce^{3+} order.

By comparison, the size of the atomic displacement parameters, to which neutron scattering is particularly sensitive, have been recently shown to relate to the quantum efficiency of a phosphor.[4] Rietveld co-refinements of the synchrotron X-ray scattering results (Figure 3a) with time-of-flight neutron data in Figure 3b enable accurate refinements of atomic displacement parameters (ADPs) of the $CaSc_2O_4$ host. The refined atomic positions and ADPs for $Ca_{0.995}Ce_{0.005}Sc_2O_4$, shown in Table 2, indicate the ADPs have magnitudes similar to those found in the highly efficient phosphors like YAG:Ce^{3+} [4] and $La_3Si_6N_{11}$:Ce^{3+}.[39] This suggests that the $CaSc_2O_4$ host also provides an especially rigid matrix that is consistent with the interconnected, edge-sharing ScO_6 polyhedra. From the ADPs, an estimation of the Debye temperature (Θ_D), which correlates to a material's photoluminescent quantum yield,[6] can be calculated.[4,39] For $CaSc_2O_4$, Θ_D is estimated to be around 900 K from the neutron data. The surprisingly high Θ_D predicted here may arise from the correlation between the strong neutron absorption of Sc^{3+} and the Rietveld refinements of the atomic displacement parameters in the method, which can lead to an overestimation of the ADP values. On the other hand, even the refined ADPs from X-ray diffraction, which is relatively insensitive to light atoms, such as oxygen, still leads to high Debye temperatures ranging between 766 K and 790 K for this system. As a result, it reasonable to estimate that Θ_D for this phosphor host ranges between 700 K and 900 K, which is substantially higher than for other high efficiency phosphors, such as YAG:Ce^{3+}[4] and $La_3Si_6N_{11}$:Ce^{3+}.[39]

Table 2. Atomic positions and atomic displacement factors (U_{iso}) refined from a combined Rietveld refinement of synchrotron X-ray and neutron powder diffraction data for $Ca_{0.995}Ce_{0.005}Sc_2O_4$.[a]

Atom	Occupancy	*x*	*y*	*Z*	$U_{iso} \times 100$
Ca	0.995	0.75651(8)	0.65237(6)	¼	0.37(1)
Ce	0.005	0.75651(8)	0.65237(6)	¼	0.37(1)
Sc(1)	1	0.41954(4)	0.10734(3)	¼	0.724(7)
Sc(2)	1	0.42962(3)	0.61213(3)	¼	0.425(6)
O(1)	1	0.20759(6)	0.17154(5)	¼	0.20(1)
O(2)	1	0.12316(5)	0.47756(5)	¼	0.16(1)
O(3)	1	0.52058(7)	0.78409(5)	¼	0.20(1)
O(4)	1	0.42058(7)	0.42464(5)	¼	0.12(1)

[a] The occupancy ratio Ca^{2+}/Ce^{3+} was held constant.

The high Debye temperature Θ_D of $CaSc_2O_4$ is corroborated by density functional theory (DFT), which provides a robust approximation based on the elastic constants (C_{ij}), as has been previously shown.[6] Here, the elastic constants for the unsubstituted $CaSc_2O_4$ are calculated by using the Vienna *ab initio* simulation package (VASP)[40,41] employing the Perdew-Burke-Ernzerhof generalized gradient approximation (PBE-GGA) to describe exchange and correlation.[42] The Debye temperature from DFT is predicted to be 694 K, which is in agreement with the range of Θ_D determined experimentally. The combination of experimental and computational results support the rigidity of the calcium scandate host structure that leads to its high PLQY.[6]

Local structures near Ce^{3+} dopants. The optical properties of rare-earth-substituted compounds are strongly affected by their local coordination environments, which result in different crystal field splittings.[3] However, because the substitution of the rare-earth ions occurs at such a low loadings (often <3%), any local distortions that occur are challenging to observe by scattering analyses of long-range order. By comparison, solid-state NMR is sensitive to local bonding environments and is also element selective. For the case of $Ca_{1-x}Ce_xSc_2O_4$, the effects of even dilute quantities of Ce^{3+} incorporated into the calcium scandate structure can be probed by using solid-state ^{45}Sc and ^{43}Ca NMR to detect displacements of signals and reduced spin-lattice relaxation

times that are induced by nearby paramagnetic Ce^{3+}. Such effects have been previously used to characterize local compositions and structures near paramagnetic species in pyrochlores,[43] stannates,[44] garnets,[4] and lanthanide-binding proteins.[45]

Starting first with the undoped parent material, the two crystallographically distinct Sc(1) and Sc(2) scandium sites in $CaSc_2O_4$ are clearly distinguished in 2D ^{45}Sc NMR measurements conducted at very high magnetic field (23.5 Tesla). Although the two signals overlap in a conventional 1D ^{45}Sc MAS spectrum (Supporting Information, Figure S1, consistent with similar analyses[46] conducted at lower field, 11.7 Tesla), they are well-resolved in the 2D *z*-filtered ^{45}Sc triple-quantum (3Q) MAS NMR spectrum in Figure 4. This spectrum was acquired under very-high field conditions (23.5 Tesla), which mitigate contributions from anisotropic second-order quadrupolar interactions that are associated with the spin $I = 7/2$ ^{45}Sc nuclei, yielding resolved signals from the two distinct ^{45}Sc sites. The 2D ^{45}Sc MQ-MAS spectrum correlates anisotropic (MAS) and isotropic spectra, from which the isotropic ^{45}Sc chemical shift (δ_{iso}), the quadrupolar coupling constant (C_Q) and the quadrupolar asymmetry parameter (η_Q) were extracted for each of the two ^{45}Sc sites by fits of each of the signals in their respective isotropic and anisotropic dimensions. These results (which are summarized in Table 3) enable the assignments of the two signals to scandium sites Sc(1) and Sc(2) and provide insights on the local coordination environments of the ^{45}Sc atoms in $CaSc_2O_4$. Specifically, site Sc(1) is assigned to the lower frequency ^{45}Sc signal with an isotropic chemical shift of 154 ppm and C_Q and η_Q values of 8.8 MHz and 0.50, respectively. The second ^{45}Sc signal with the isotropic chemical shift of 157 ppm, a larger C_Q of 14.3 MHz, and η_Q of 0.76, is assigned to Sc(2). The larger C_Q value is consistent with the less symmetric local bonding environment of Sc(2), in line with the scattering analyses (Figure 3 and Table 1). The minor deviation of the fitted lineshape near the center (ca. 147 ppm) of the experimental spectrum for Sc(2) (slice *ii*) is associated with uncertainty in the fitted value of η_Q and reflects well-known difficulties in obtaining precise values

of this parameter. Nevertheless, the singularities at the edges of the lineshape, which are associated with the value of C_Q, are reproduced with a high degree of precision. These results are also consistent with the larger bond-angle variance of 78° for site Sc(2), compared with 29° for Sc(1), as determined by Rietveld refinement of the scattering data above.

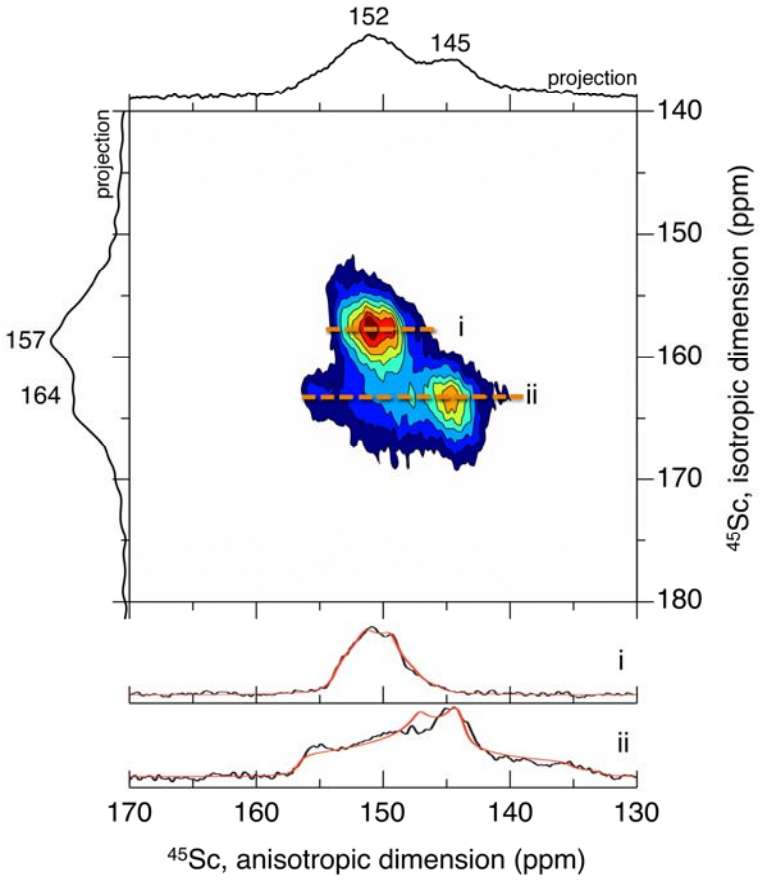

Figure 4. Solid-state ^{45}Sc *z*-filtered triple-quantum MAS spectrum of $CaSc_2O_4$ acquired at 23.5 T under MAS conditions of 60 kHz and at approximately 360 K. Projections are shown along the corresponding anisotropic and isotropic axes. Horizontal slices (i) and (ii) are extracted from the isotropic dimension, as indicated by the orange dashed lines. Fits to the extracted spectra are shown as red lines. The sample is the same as used in Figures 5 and 6.

Table 3. ^{45}Sc isotropic chemical shifts, quadrupolar coupling constants, and asymmetry parameters for the two scandium sites in crystalline $CaSc_2O_4$.[a]

atom	δ_{iso} (ppm)	C_Q (MHz)	η_Q
Sc(1)	154 ± 0.5	8.8 ± 0.1	0.50 ± 0.1
Sc(2)	157 ± 0.5	14.3 ± 0.1	0.76 ± 0.15

[a] Table values were determined from fits to slices in the isotropic dimension of the ^{45}Sc MQ-MAS spectrum in Figure 4.

The incorporation of Ce^{3+} ions into the calcium scandate structure influences the local environments of nearby scandium sites, even for low extents of Ce^{3+} substitution. This is evident in the solid-state 1D ^{45}Sc MAS NMR spectra acquired at 360 K in Figure 5 for $Ca_{1-x}Ce_xSc_2O_4$ with Ce^{3+} substitutions for Ca^{2+} cations in the range of 0-1.5%. The ^{45}Sc MAS spectrum for the undoped $CaSc_2O_4$ (x = 0) material exhibits a complicated lineshape in Figure 5a(top), because it contains the two overlapping central transition signals that were resolved in the 2D ^{45}Sc MQ-MAS spectrum, as well as two signals due to the centerbands of the satellite-transitions spinning side-band manifolds that are also associated with each of the two scandium sites. As small quantities of Ce^{3+} are incorporated into $Ca_{1-x}Ce_xSc_2O_4$, new weak ^{45}Sc signals appear at approximately 177 ppm and 205 ppm, both of which increase in intensity with the extent of Ce^{3+} substitution and which are assigned to scandium sites Sc(1) and Sc(2), respectively, based on their relative shifts. The ^{45}Sc signal near 177 ppm appears to partially overlap with the satellite transition at ca. 174 ppm, the latter's intensity and position of which remain constant with Ce^{3+} substitution and temperature. It is noteworthy that the positions of the signals at 177 and 205 ppm exhibit marked temperature dependences and are further displaced to 180 and 208 ppm, respectively, at 300 K (blue trace in Figure 5b). The displacements of the signals to higher chemical shifts at lower temperatures are consistent with the inverse temperature dependence of paramagnetic shifts associated with the Fermi contact and spin-dipolar (pseudo-contact) interactions of the ^{45}Sc nuclei with the nearby paramagnetic Ce^{3+} cations.[44,47] In addition, the ^{45}Sc spin-lattice relaxation time (T_1) associated with the non-displaced dominant signal at ca. 150 ppm decreases monotonically from 11 s to 8.7 s as the Ce^{3+} substitution for Ca^{2+} increases from 0% to 1.5%. This is consistent with induced paramagnetic relaxation enhancement[48] of the ^{45}Sc polarization, due to long-range dipolar couplings to distant (> 1 nm) paramagnetic Ce^{3+} cations. The widths of the non-displaced ^{45}Sc peaks also increase with Ce^{3+} substitution, reflecting (1) an increased concentration of local distortions in the lattice, (2) an

increase in the anisotropic bulk magnetic susceptibility broadening,[49] and (3) the decrease in the overall transverse relaxation time constant associated with the increased Ce^{3+} content. More importantly, the ^{45}Sc T_1 value associated with the weak resolved signal at 205 ppm was measured to be approximately 140 ms, which is almost two orders of magnitude shorter than for the ^{45}Sc sites in bulk undoped $CaSc_2O_4$. Although a reliable quantitative fit of the T_1 of the peak at 177 ppm is more difficult to obtain, due to the overlap with the satellite transition, we estimate an approximate value of 200-300 ms. These substantially shorter T_1 values are consistent with paramagnetic-relaxation-enhancement effects that arise from the short-range interactions of ^{45}Sc atoms with nearby paramagnetic Ce^{3+} ions that increase with dopant loading.

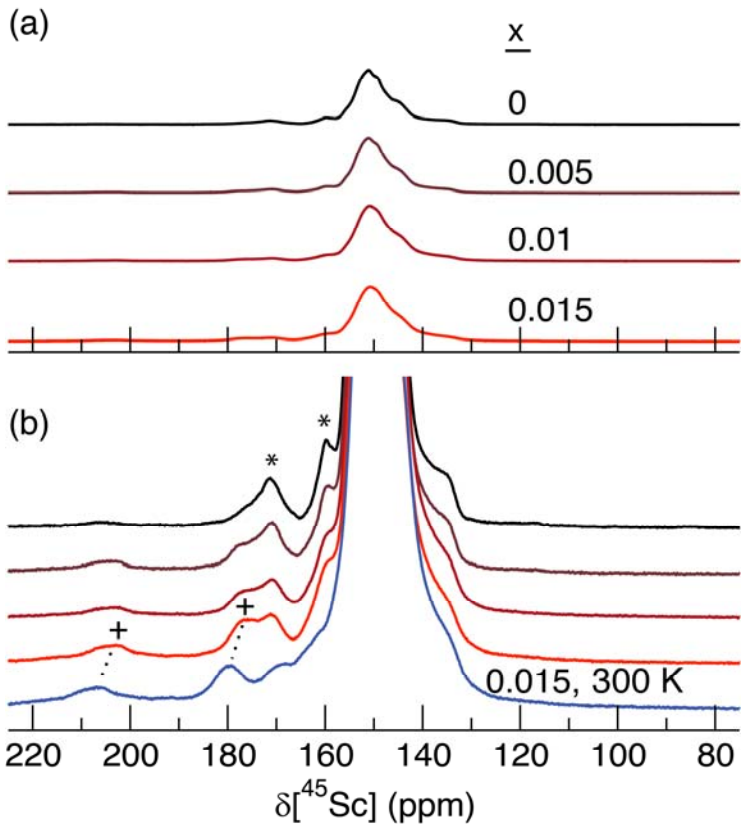

Figure 5. (a) Solid-state single-pulse ^{45}Sc MAS NMR spectra of $Ca_{1-x}Ce_xSc_2O_4$ with different Ce^{3+} compositions (x) acquired at 23.5 T and 60 kHz MAS, recycle delay of 0.1 s, with and approximately 360 K. (b) The data are shown with a vertical expansion of the spectra by a factor of 100. Signals from satellite transitions are marked by asterisks (see Supporting Information, Figure S1), and paramagnetically displaced peaks are indicated with "+" symbols. The effect of temperature on the paramagnetic displacement at 300 K magnitude is highlighted by dashed lines as a guide for the eye. The samples are the same as used in Figures 2, 3, 4, 6, and 7.

The incorporation of Ce^{3+} dopant ions into $Ca_{1-x}Ce_xSc_2O_4$ materials is also evident in the effects on nearby unsubstituted Ca^{2+} sites. As shown in Figure 6a, the 1D solid-state ^{43}Ca MAS NMR spectrum of undoped $CaSc_2O_4$ reveals a single relatively narrow signal at 62 ppm with a full-width at half-maximum (fwhm) of 3 ppm. This indicates the presence of a single well-defined Ca^{2+} site which is consistent with the long-range crystalline order of the $CaSc_2O_4$ parent material. For the Ce^{3+}-doped materials, an additional feature appears at approximately 70 ppm. The large displacement of this new signal with respect to the main peak is a consequence of long-range spin-dipolar interactions of the ^{43}Ca nuclei with nearby paramagnetic Ce^{3+} dopant species, and its broader linewidth (ca. 12 ppm fwhm) is consistent with a progressively weaker paramagnetic effect sensed by $^{43}Ca^{2+}$ cations in successive coordination spheres. Given the extremely long T_1 of the $^{43}Ca^{2+}$ nuclei, both these signals were saturated during the NMR experiment, preventing quantitative analysis of their relative intensities.

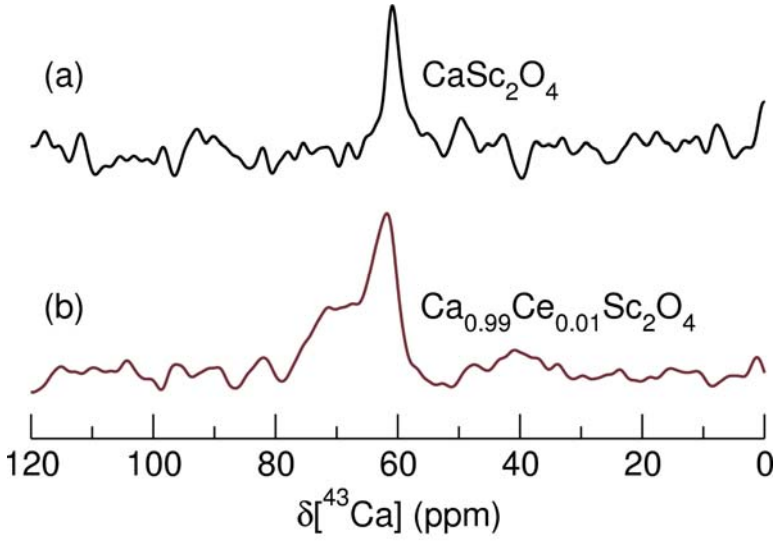

Figure 6. Solid-state single-pulse ^{43}Ca MAS NMR spectra of $Ca_{1-x}Ce_xSc_2O_4$ phosphor materials with different Ce^{3+} dopant compositions acquired at room temperature at 19.6 T, 7 kHz MAS, and with a 5 s recycle delay: (a) undoped $CaSc_2O_4$ and (b) $Ca_{0.99}Ce_{0.01}Sc_2O_4$. The samples are the same as used in Figures 4 and 5.

Ce^{3+} local structure from EPR. Although NMR can indirectly provide details on local structural features of atoms near the Ce^{3+} cations, electron paramagnetic resonance (EPR) spectroscopy probes the paramagnetic Ce^{3+} species directly. The splitting of the fundamental $^2F_{5/2}$ electron energy levels by the crystal field reduces the spin system to an effective $S = 1/2$ spin system with an anisotropic g factor. EPR spectra are shown in Figure 7 for several otherwise identical Ce^{3+}-doped calcium scandates ($Ca_{1-x}Ce_xSc_2O_4$), except for their different extents of Ce^{3+} substitution (x = 0.005, 0.01, 0.015). In each of the EPR spectra, the vast majority of the intensity (90%) is associated with one type of Ce^{3+} site with rhombic symmetry that yields three signal components at g_{1x} = 2.70 (2500 G), g_{1y} = 1.62 (4100 G), and g_{1z} = 1.33 (5100 G). This range of g tensors is smaller than those reported for YAG:Ce^{3+}, (g_x = 2.73 and g_z = 0.908),[4] and reflects smaller crystal-field splittings in the $Ca_{1-x}Ce_xSc_2O_4$ materials. Interestingly, a second Ce^{3+} site also appears to be present, corresponding to three much weaker Ce^{3+} signals at g_{2x} = 2.38 (2800 G), g_{2y} = 2.07 (3100 G), and g_{2z} = 1.40 (4100 G) that account for 9% of the total signal intensity. This second Ce^{3+} signal may arise from Ce^{3+} ions in or near distorted Ca^{2+} sites, which would be consistent with the broad ^{43}Ca signal at ca. 70 ppm in the ^{43}Ca MAS NMR spectrum of Figure 6b. Figure 7a shows a fit to the EPR spectrum acquired for the material with the

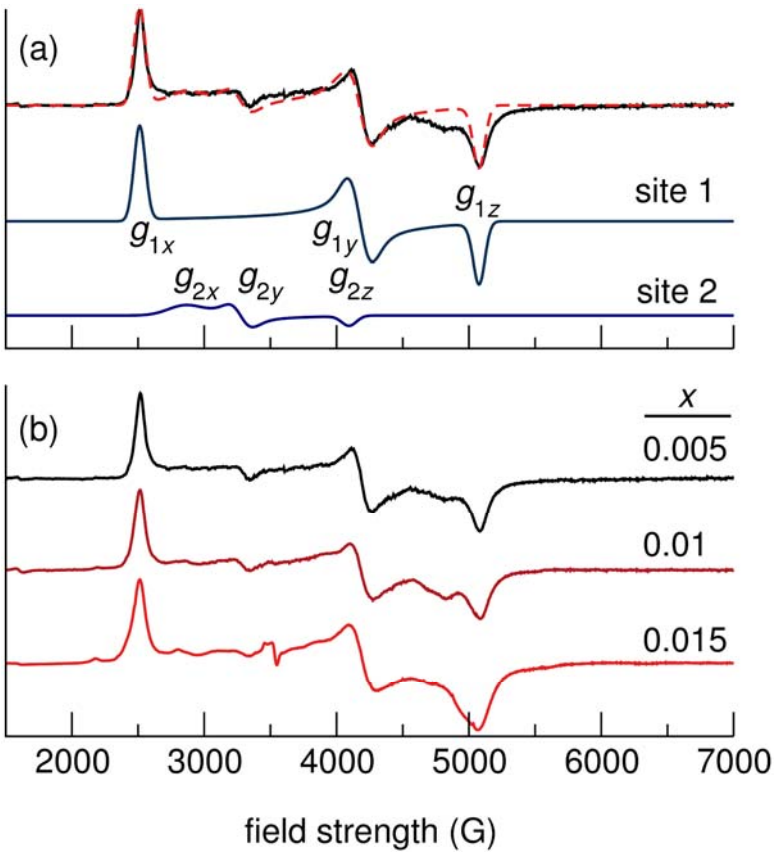

Figure 7. (a) Powder EPR spectrum (black solid line) and accompanying fit (red dashed line) for the phosphor composition $Ca_{0.995}Ce_{0.005}Sc_2O_4$ (x = 0.005), with evidence of two distinct Ce^{3+} sites: site 1 (light blue) and site 2 (dark blue). (b) EPR spectra acquired at 4 K and 9.4 GHz of Ce^{3+} in $Ca_{1-x}Ce_xSc_2O_4$ for x = 0.005, 0.01, 0.015. The samples are the same as used in Figures 2, 3, 5, and 6.

composition $Ca_{0.995}Ce_{0.005}Sc_2O_4$, corresponding to the phosphor with the superior photoluminescence properties. The dashed red line in Figure 7a is a summation of weighted contributions of the two individual fits shown and is in good agreement with the experimental spectrum, indicating that most of the features in the spectrum are accounted for by the two types of Ce^{3+} sites in the doped calcium scandate structure. A small spectral feature remains near 4800 G. Because the synchrotron X-ray powder diffraction data did not indicate the presence of significant crystalline impurity phases, this may be from an additional distorted of Ce^{3+} site or associated with a minor amount of disordered or defect species. As the concentration of Ce^{3+} increases, this feature near 4800 G becomes more prominent, as shown in Figure 7b; however, attempts to fit this signal by including a third Ce^{3+} site were unsuccessful. Nevertheless, as distortions occur with Ce^{3+}

incorporation, the probability of non-radiative relaxation increases and can explain the rapid decrease in quantum efficiency with increased Ce^{3+} content.

CONCLUSIONS

Cerium-doped $CaSc_2O_4$ has been shown to be a phosphor that possesses a rigid host crystal structure, as manifested by its high Debye temperature (>700 K), based on scattering measurements and DFT calculations. The high structural rigidity is correlated to the high photoluminescent quantum yield of over 80% for $Ca_{0.995}Ce_{0.005}Sc_2O_4$ (0.5% Ce^{3+} substitution for Ca^{2+}), as well as the temperature stability of the luminescence emission. Interestingly, the quantum yield is very sensitive to the extent of cerium incorporation, dropping abruptly to 45%, as the Ce^{3+} substitution approaches 1.5%. Variable-temperature solid-state ^{45}Sc NMR measurements establish that the decrease in quantum yield is correlated with paramagnetic displacements of ^{45}Sc signals that are associated with scandium sites Sc(1) and Sc(2) near very dilute paramagnetic Ce^{3+} dopant ions in $Ca_{1-x}Ce_xSc_2O_4$. Direct EPR measurements of the Ce^{3+} ions reveal two types of Ce^{3+} sites, one relatively ordered site that accounts for approximately 90% of the Ce^{3+} ions in the in $Ca_{1-x}Ce_xSc_2O_4$ materials, and the other corresponding to ~9% of more distorted Ce^{3+} sites. The EPR spectra indicate that this fraction of distorted Ce^{3+} sites increases with Ce^{3+} loading and correlates well with the decrease in quantum efficiency for Ce^{3+} substitutions above 0.5%. Overall, the combined scattering, solid-state ^{45}Sc and ^{43}Ca NMR, EPR, and DFT analyses yield detailed new understanding of the structure-property correlations that are associated with the technologically promising green-emitting phosphor, $Ca_{0.995}Ce_{0.005}Sc_2O_4$. The results provide insights and design criteria that are expected to be useful for the discovery, optimization, and development of novel and efficient phosphor materials for optoelectronics or solid-state lighting applications.

Acknowledgements

The authors thank J. Siewenie for assistance with collection of the neutron powder diffraction data and Dr. Z. Gan for assistance with the ^{43}Ca NMR measurements. The work at the ENS-Lyon was supported by the Initial Training Network on paramagnetic NMR funded by the European Union's Seventh Framework Program for research, technological development and demonstration (FP7-PEOPLE-2012-ITN contract n. 317127 "pNMR"). N.C.G. acknowledges support from the ConvEne IGERT Program of the U. S. National Science Foundation (NSF-DGE 0801627). A.J.P. and G.P. were supported by the LABEX iMUST (ANR-10-LABX-0064) of the Université de Lyon, within the program "Investissements d'Avenir" (ANR-11-IDEX-0007) operated by the Agence Nationale de la Recherche (ANR). The research made extensive use of the Central Facilities of the UCSB Materials Research Laboratory, supported by the MRSEC Program of the NSF under Award DMR-1121053, which is a member of the NSF-funded Materials Research Facilities Network (www.mrfn.org). Use of the Advanced Photon Source at Argonne National Laboratory was supported by the U. S. Department of Energy, Office of Science, Office of Basic Energy Sciences, under Contract No. DE-AC02-06CH11357. This work benefited from the use of the HIPD beamline at the Lujan Center at Los Alamos National Laboratory, funded by the DOE Office of Basic Energy Sciences; LANL is operated by Los Alamos National Security LLC under DE-AC52-06NA25396. The solid-state NMR measurements at 23.5 T were conducted at the Centre Européen de Résonance Magnétique Nucléaire à Très Hauts Champs in Lyon, France. Solid-state ^{43}Ca NMR measurements were conducted at the U.S. National High Magnetic Field Laboratory, Tallahassee, Florida, supported by the U.S. NSF. B.F.C. thanks the ENS-Lyon for support as a "Professeur Invité" in 2013.

Supporting Information Available

The following material is available free of charge via the Internet at http://pubs.acs.org: first-principles calculation methods, solid-state single-pulse ^{45}Sc MAS NMR spectra for $CaSc_2O_4$

(without Ce dopant species), the emission profiles measured for different $Ca_{1-x}Ce_xSc_2O_4$ materials with different cerium contents (x=0.005, 0.0075, 0.01, and 0.015), the temperature-dependent PL spectra for $Ca_{1.995}Ce_{0.005}Sc_2O_4$.

References

1. Service, R. F. The Quest for White LEDs Hits the Home Stretch. *Science*, **2009**, *325*, 809-809.

2. Pimputkar, S.; Speck, J. S.; DenBaars, S. P.; Nakamura, S. Prospects for LED lighting. *Nature Photon.*, **2009**, *3*, 180-182.

3. George, N. C.; Denault, K. A.; Seshadri, R. Phosphors for Solid-State White Lighting, *Ann. Rev. Mater. Res.*, **2013**, *43*, 481-501.

4. George, N. C.; Pell, A. J.; Dantelle, G.; Page, K.; Llobet, A.; Balasubramanian, M.; Pintacuda, G.; Chmelka, B. F.; Seshadri, R. Local Environments of Dilute Activator Ions in the Solid-State Lighting Phosphor $Y_3Al_5O_{12}$, *Chem. Mater.*, **2013**, *25*, 3979-3995.

5. Höppe, H. A. Recent Developments in the Field of Inorganic Phosphors. *Angew. Chem. Int. Edit.*, **2009**, *48*, 3572-3582.

6. Brgoch, J.; DenBaars, S. P.; Seshadri, R. Proxies from *ab-initio* Calculations for Screening Efficient Ce^{3+} Phosphor Hosts. *J. Phys. Chem. C*, **2013**, *117*, 17955-17959.

7. Philippen, J.; Guguschev, C.; Bertram, R.; Klimm, D. Laser-Heated Pedestal Growth of Cerium Doped Calcium Scandate Crystal Fibers. *J. Cryst. Growth*, **2013**, *363*, 270-276.

8. Klimm, D., Philippen, J.; Markurt, T.; Kwansneiwski, A. Ce^{3+}:$CaSc_2O_4$ Crystal Fibers for Green Light Emission: Growth Issues and Characterization. *MRS Proc.* **2014**, *1655*.

9. Peng, W.; Zou, S.; Liu, G.; Xiao, Q.; Meng J.; Zhang, R. Combustion Synthesis and Upconversion Luminescence of $CaSc_2O_4$:Yb^{3+},Er^{3+} Nanopowders. *J. Rare Earth.*, **2011**, *29*, 330-334.

10. Chen, Y.; Cheah, K. W.; Gong, M. Low Temperature Quenching and High Efficiency Tm^{3+}, La^{3+} or Tb^{3+} Co-Doped $CaSc_2O_4$:Ce^{3+} Phosphors for Light-Emitting Diodes. *J. Lumin.*, **2011**, *131*, 1770-1775.

11. Zhijun, W.; Zhi, T.; Jianqi, Y.; Xian, S.; Shuai, Q.; Yamin, L.; Zhiping, Y.; Panlai, L.; Zhenu, X. Recent Development on Single-Phase White Emitting Phosphors for White LEDs. *J. Chin. Ceram. Soc.,* **2016**, *44*, 1.

12. Georgescu, S.; Stefan, A.; Toma, O. Judd–Ofelt and Energy-Transfer Analysis of Er^{3+} Doped in $CaSc_2O_4$ Ceramic Samples. *J. Lumin.,* **2015**, *167*, 186-192.

13. Georgescu, S.; Stefan, A.; Toma, O.; Voiculescu, A.-M. Judd–Ofelt Analysis of Ho^{3+} Doped in Ceramic $CaSc_2O_4$. *J. Lumin.,* **2015**, *162*, 174-179.

14. Georgescu, S.; Stefan, A.; Voiculescu, A.-M.; Toma, O. Judd–Ofelt Analysis of Tm^{3+} doped in $CaSc_2O_4$ Ceramic Samples. *J. Lumin.,* **2015**, *166*, 130-136.

15. Chen, Y.; Ni, H., Cheah, K. W.; Gong, M. Low Temperature Quenching and High Efficiency Tm^{3+}, La^{3+} or Tb^{3+} Co-Doped $CaSc_2O_4$:Ce^{3+} Phosphors for Light-Emitting Diodes. *J. Lumin.,* **2011**, *131*, 1770-1775.

16. Li, J.; Hao, Z.; Zhang, X.; Zhang, L.; Luo, Y.; Zhang, J. Efficient Near-Infrared Downconversion and Energy Transfer Mechanism of Ce^{3+}/Yb^{3+} Codoped Calcium Scandate Phosphor. *Inorg. Chem.,* **2015**, *54*, 4806-4810.

17. Li, J.; Zhang, J.; Hao, Z.; Zhang, X.; Zhao, J.; Luo, Y. Spectroscopic Properties and Upconversion Studies in Ho^{3+}/Yb^{3+} Co-doped Calcium Scandate with Spectrally Pure Green emission. *ChemPhysChem,* **2013**, *14*, 4114-4120.

18. Li, J.; Zhang, J.; Hao, Z.; Chen, L.; Zhang, X.; Luo, Y. Intense Upconversion Luminescence of $CaSc_2O_4$:Ho^{3+}/Yb^{3+} from Large Absorption Cross Section and Energy-Transfer Rate of Yb^{3+}. *ChemPhysChem,* **2015**, *16*, 1366-1369.

19. Li, J.; Zhang, J.; Hao, Z.; Zhang, X.; Zhao, J.; Luo, Y. Upconversion Properties and Dynamics Study in Tm^{3+} and Yb^{3+} Codoped $CaSc_2O_4$ Oxide Material. *J. Appl. Phys.,* **2013**, *113*, 223507.

20. Li, J.; Zhang, J.; Hao, Z.; Zhang, X.; Zhao, J.; Lu, S.; Luo, Y. Synthesis, Morphology, and Upconversion Luminescence of Tm^{3+}/Yb^{3+} Codoped Bulk and Submicro-Rod $CaSc_2O_4$ phosphors. *Inorg. Chem. Comm.,* **2013**, *38*, 119-122.

21. Müller-Buschbaum, H.; Schnering, H. G. Über Oxoscandate. I. Zur Kenntnis des $CaSc_2O_4$. *Z. Anorg. Allg. Chem.*, **1965**, *336*, 295–305.

22. Shimomura, Y.; Kurushima, T.; Kijima, N. Photoluminescence and Crystal Structure of Green-Emitting Phosphor $CaSc_2O_4$:Ce^{3+}. *J. Electrochem. Soc.*, **2007**, *154*, J234-J238.

23. Shannon, R. D. Revised Effective Ionic Radii and Systematic Studies of Interatomic Distances in Halides and Chalcogenides. *Acta Crystallogr. A*, **1976**, *32*, 751-767.

24. Kalaji, A.; Mikami, M.; Cheetham, A. K. Ce^{3+}-Activated γ-Ca_2SiO_4 and Other Olivine-Type $ABXO_4$ Phosphors for Solid-State Lighting. *Chem. Mater.*, **2014**, 26 (13), 3966–3975.

25. de Mello, J. C.; Wittmann, H. F.; Friend, R. H. An Improved Experimental Determination of External Photoluminescence QuantumEfficiency. *Adv. Mater.*, **1997**, *9*, 230-232.

26. Wang, J.; Toby, B. H.; Lee, P. L.; Ribaud, L.; Antao, S. M.; Kurtz, C.; Ramanathan, M.; Von Dreele, R. B.; Beno, M. A. A Dedicated Powder Diffraction Beamline at the Advanced Photon Source: Commissioning and Early Operational Results. *Rev. Sci. Instrum.*, **2008**, *79*, 0851050-0851057.

27. Toby, B. H. *EXPGUI*, a Graphical User Interface for *GSAS*. *J. Appl. Cryst.*, **2001**, *34*, 210-213.

28. Larson, A. C.; Dreele, R. B. V. General Structure Analysis System (GSAS). *Los Alamos National Laboratory Report* LAUR 86-7482000.

29. Momma, K.; Izumi, F. VESTA 3 for Three-Dimensional Visualization of Crystal, Volumetric and Morphology data. *J. Appl. Crystallogr.*, **2011**, *44*, 1272-1276.

30. Medek, A.; Harwood, J. S.; Frydman, L. Multiple-Quantum Magic-Angle Spinning NMR: A New Method for the Study of Quadrupolar Nuclei in Solids. *J. Am. Chem. Soc.*, **1995**, *117*, 12779-12787.

31. Amoureux, J.-P.; Fernandez, C.; Steuernagel, S. *J.* Z Filtering in MQMAS NMR. *Magn. Reson. Ser. A*, **1996**, *123*, 116-118.

32. States, D. J.; Haberkorn, R. A.; Ruben, D. J. A Two-Dimensional Nuclear Overhauser Experiment with Pure Absorption Phase in Four Quadrants. *J. Magn. Reson.*, **1982**, *48*, 286-292.

33. Grandinetti, P. J.; Ash, J. T.; Trease, N. M. Symmetry Pathways in Solid-State NMR. *Prog. Nucl. Mag. Res. Spectr.*, **2011**, *59*, 121-196.

34. Massiot, D.; Fayon, F.; Capron, M.; King, I.; Le Calvé, S.; Alonso, B.; Durand, J. O.; Bujoli, B.; Gan, Z.; Hoatson, G. Modelling One and Two-Dimensional Solid-State NMR spectra. *Magn. Reson. Chem.*, **2002**, *40*, 70-76.

35. Stoll, S.; Schweiger, A. EasySpin, a Comprehensive Software Package for Spectral Simulation and Analysis in EPR. *J. Magn. Reson.*, **2006**, *178*, 42-55.

36. Shimomura, Y.; Honma, T.; Shigeiwa, M.; Akai, T.; Okamoto, K; Kijima, N. Photoluminescence and Crystal Structure of Green-Emitting $Ca_3Sc_2Si_3O_{12}$:Ce^{3+} Phosphor for White Light Emitting Diodes. *J. Electrochem. Soc.*, **2007**, *154*, J35-J38.

37. Carter, J. R.; Feigelson, R. S. Preparation and Crystallographic Properties of $A^{2+}B_2^{3+}O_4$, Type Calcium and Strontium Scandates. *J. Am. Ceram. Soc.*, **1964**, *47*, 141–144.

38. Horyn, R.; Lukaszewicz, K. B. Refinement of the Crystal Structure $CaCsO_4$, *Acad. Pol. Sci.-Chim.*, **1966**, 499-504.

39. George, N. C.; Birkel, A.; Brgoch, J.; Hong, B.-C.; Mikhailovsky, A. A.; Page, K.; Llobet, A.; Seshadri, R. Average and Local Structural Origins of the Optical Properties of the Nitride Phosphor $La_{3-x}Ce_xSi_6N_{11}$($0<x\leq3$). *Inorg. Chem.*, **2013**, *52*, 13730-13741.

40. Kresse, G.; Furthmuller, J. Ab Initio Molecular Dynamics for Liquid Metals. *Phys. Rev. B*, **1993**, *47*, 558-561.

41. Kresse, G.; Furthmuller, J. Efficient Iterative Schemes for Ab Initio Total-Energy Calculations Using a Plane-Wave Basis Set. *Phys. Rev. B*, **1996**, *54*, 11169-11186.

42. Perdew, J. P.; Burke, K.; Ernzerhof, M. Generalized Gradient Approximation Made Simple. *Phys. Rev. Lett.*, **1996**, *77*, 3865-3868.

43. Cheetham, A. K.; Dobson, C. M.; Grey, C. P.; Jakeman, R. J. B. Paramagnetic Shift Probes in High-Resolution Solid-State NMR. *Nature*, **1987**, *328*, 706-707.

44. Grey, C. P.; Dobson, C. M.; Cheetham, A. K.; Jakeman, R. J. B. Studies of Rare-Earth Stannates by ^{119}Sn MAS NMR. The Use of Paramagnetic Shift Probes in the Solid State. *J. Am. Chem. Soc.*, **1989**, *111*, 505-511.

45. Pintacuda, G.; John, M.; Su, X. C.; Otting, G. NMR Structure Determination of Protein–Ligand Complexes by Lanthanide Labeling. *Acc. Chem. Res.*, **2007**, *40*, 206-212.

46. Bräuniger, T.; Hofmann, A. J.; Moudrakovski, I. L.; Hoch, C.; Schnick, W. A ^{45}Sc-NMR and DFT Calculation Study of Crystalline Scandium Compounds. *Solid State Sci.,* **2016**, *51*, 1-7.

47. Bleaney, B. Nuclear Magnetic Resonance Shifts in Solution Due to Lanthanide Ions. *J. Mag. Reson.*, **1972**, *8*, 91-100.

48. Pell, A. J.; Pintacuda, G. Broadband Solid-State MAS NMR of Paramagnetic Systems. *Prog. Nucl. Magn. Reson. Spectr.*, **2015**, *84-85*, 33-72.

49. Alla, M.; Lippmaa, E. Resolution Limits in Magic-Angle Rotation NMR Spectra of Polycrystalline Solids. *Chem. Phys. Lett.*, **1982**, *87*, 30-33.

TOC Graphic:

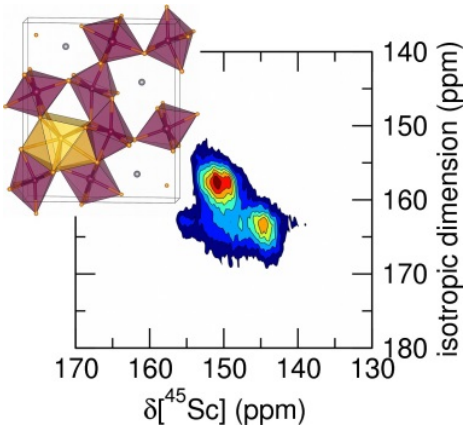
140
150
160
170
180
isotropic dimension (ppm)
170
160
150
140
130
δ[45Sc] (ppm)